Effect of Electrolytes on Electrochemical Properties of MmNi$_5$-based Hydrogen Storage Alloy

Chengyuan Ni[1,], Huaiying Zhou[2,*], Zhongmin Wang[2], Qingrong Yao[2], Lanying Lu[3]*

[1] School of Mechanical Engineering, Quzhou University, Quzhou, Zhejiang 324000, China
[2] School of Materials Science and Engineering, Guilin University of Electronic Technology, Guilin, Guangxi 541004, China
[3] School of Chemistry, University of St. Andrews, North Haugh, St Andrews, Fife, KY16 9ST, Scotland, United Kingdom
[*]E-mail: nichengyuan1@126.com; zhy@guet.edu.cn

The effect of electrolytes on the electrochemical properties of MmNi$_{3.68}$Co$_{0.72}$Mn$_{0.43}$Al$_{0.17}$ hydrogen storage alloy electrodes has been investigated at 303 K and 273 K. Three electrolytes (EL1, EL2, EL3) were obtained by adding 2 wt%, 4 wt% and 6 wt% LiOH into the original electrolyte EO (6 M/L KOH), respectively. The results indicate that the addition of LiOH improves the discharge capacity and cycle life at 303 K and 273 K. The highest maximum capacity and capacity retention (after 50th cycles) have been observed in electrolyte EL2. However, the high-rate dischargeability (HRD) decreases gradually from EO to EL3 at the two temperatures because of the addition of LiOH. The corrosion current I_{corr} from Tafel Polarization curves (*TP*) and the resistance of the oxide layer R_{ol} from electrochemical impedance spectroscopy (*EIS*) indicates that the alloy electrode worked in EL1 has a better anti-corrosion ability. The real surface area of the electrodes estimated with *EIS* analysis, decrease from 51.95 cm^2 in EO to 15.6 cm^2 in EL2, but increase to 31.59 cm^2 in EL3 after being fully activated. The additional LiOH improves the anti-pulverization ability of alloy powders, delay the loss of active elements within the alloy electrode, resulting in an inproved capacity retention of alloy electrode. Meanwhile, the electrochemical kinetics analysis suggests that the charge-transfer reaction at the interface of electrode surface and electrolyte is the rate-determining step when tested at 303 K and 273 K.

Keywords: Hydrogen storage alloy; Electrolyte; pulverization characteristic; Capacity degradation; Electrochemical kinetics.

1. INTRODUCTION

Nickel/metal hydride (Ni/MH) secondary batteries using AB$_5$-type hydrogen storage alloys as negative electrode materials have been widely employed in portable electrical devices and power

sources due to their high energy density, environmental friendliness and interchangeability compared with nickel/cadmium batteries. But in recent years, Ni/MH battery is encountering serious competition from Li-ion batteries and other advanced secondary batteries. It is more and more urgent to reduce production cost and improve the capacity and cycle life of Ni/MH batteries to enhance their competition in the rechargeable battery market.

In the past decade, much work has been invested to develop relatively low cost AB_5-type alloys for the Ni/MH battery applications. Elemental substitution is one of the most effective ways to improve the overall properties of the hydrogen storage alloys and obtain the desired properties. On the A-site, partial substitution of La by Ce or Nd in rare earth-based AB_5-type alloys generally results in a markedly increase in the equilibrium hydrogen pressure and an improvement in the anti-corrosion ability [1-3]. Misch-metal-based AB_5-type alloys are among the most extensively investigated materials for use as anodes in Ni-MH batteries because of their low cost and availability [4-7], and they exhibit long cycle life and superior performance compared to other competing materials [8-12]. Meanwhile, on the B-site, partial substitution of Ni by elements, such as Al, Mn, Cu and Fe, is beneficial to many aspects of the rare earth-based hydrogen storage alloys. For example, Partial substitution of Ni by Co or combination with Mn or Al is reported to improve the cycling stability [13]. The partial substitution of Ni with Mn increases the lattice parameters and the cell volume, while decreases the plateau equilibrium pressure. Al is beneficial to the charge and discharge efficiency and cycle life of the electrodes [14].

Besides the inherent properties of hydrogen storage alloys, studies have shown that the electrochemical properties of the Ni/MH cell depend on the absorption and desorption of hydrogen during charging and discharging [15-17], mainly resulting from an electrochemical reaction at the interface electrode-electrolyte. Therefore the electrolyte also plays an important role in the metal-hydride (MH) battery [18, 19]. In our previous investigations on the effect of electrolyte on electrochemical characteristics of $MmNi_{3.55}Co_{0.72}Al_{0.3}Mn_{0.43}$ alloy electrode [20, 21], the alloy electrodes performed good durability and high rate dischageability in the alkali electrolyte, including appropriate amounts of Al^{3+} ($Al_2(SO_4)_3$) or Mn^{2+} ($MnSO_4$). It would be interested to find out whether a similar effect occurs if appropriate amounts of other metal ion were added into the alkali electrolyte. Izawa has reported that the existence of Li in the surface could accelerate the H_2 dissociation on the surface and the penetration of H into the bulk for $LaNi_5$ alloy [22-24]. Thus by altering the composition of the electrolyte with the additional LiOH, the durability and high rate dischargeability of the electrodes may be improved.

The purpose of this study is to examine the effect of the electrolytes with various concentrations of LiOH additions on the electrochemical properties of $MmNi_5$-based hydrogen storage alloy, with the composition of our previous investigation [25]. The $MmNi_5$-based hydrogen storage alloy is fabricated using a mischmetal composed of La, Ce and Nd instead of pure lanthanum and a B-site multi-component alloying with Mn and Al. The discharge behaviors of the alloy electrodes in different electrolytes are studied at 303 K and 273 K. Meanwhile, the corrosion and pulverization characteristics of alloy electrodes in different electrolytes are analyzed using Tafel polarization and electrochemical impedance spectroscopy (*EIS*) measurement. Accordingly, the effects of electrolyte on

the electrochemical performance, especially the capacity degradations and electrochemical kinetics are overall investigated.

2. EXPERIMENTAL

2.1 Characterization of AB$_5$ type hydrogen storage alloy, and Fabrication of testing battery

The alloy with composition $MmNi_{3.68}Co_{0.72}Mn_{0.43}Al_{0.17}$, where Mm denotes La-rich mixed mischmetal composed of 58 wt% La, 25 wt% Ce, and 17 wt% Nd, was synthesized in an arc-melting furnace under argon atmosphere, and turned over and remelted several times to achieve a better homogeneity. Then, the alloy was mechanically crushed and grounded to powders below 250 meshes under a protective argon atmosphere. The X-ray diffraction (*XRD*) analysis was carried out using a D8 ADVANCED (Cu- Kα radiation) X-ray diffraction and the diffraction angles were calibrated by means of the internal silicon standard, then the lattice parameters were calculated by a software named as "Unitcell". The P–C isotherms of prepared alloy were measured by an automated Sieverts apparatus at 303 K, 323 K and 353 K.

For electrochemical measurement, all the negative electrodes were prepared by cold pressing the mixture of 0.3 g alloy powders and 0.3 g nickel powders into nickel foam sheet (1×1 cm^2). Here the commercial nickel hydroxide ($Ni(OH)_2$) was used as the counter electrode (positive). The composition of electrolytes EL1, EL2 and EL3 used in the experiment was obtained by adding 2 wt%, 4 wt% and 6 wt% LiOH to the original electrolyte EO (6 M/L KOH), respectively, as listed in Table1.

Table 1. The compositions of the electrolytes used in the experiments

Electrolyte	Compositions of electrolyte		Density (293K) (g/ ml)	Concentration of Li$^+$ (mol/ L)
	KOH (g / L)	LiOH (g / L)		
EO	336	0	1.24	0
EL1	336	7.72	1.24	0.16
EL2	336	15.42	1.25	0.32
EL3	336	20.16	1.25	0.48

2.2. Electrochemical measurement

Charge/discharge tests were carried out on a computer-controlled Kikusui PFX40W-08 battery testing instrument. In the charge/discharge tests, the electrodes were fully charged at current density of 60 mA/g for 6 h followed by 5 min rest, and then discharged at the same discharge current density to a cutoff potential of 0.9 V for 5 times till the alloy electrodes were fully activated at 303 K. Then the 273

K temperature discharge was measured after laying the testing system at constant temperature for 4h using a cooling system. In order to illustrate cycling stability, capacity retention S_{50} is calculated as:

$$S_{50} = \frac{C_{50}}{C_{max}} \times 100\% \quad (1)$$

where C_{50} is the discharge capacity at the 50th cycle, and C_{max} is the maximum discharge capacity.

High-rate discharge behavior was measured with step mode high-rate discharge method. The discharge current increased from 0.5 C to 6 C with increasing cycles. For each charge/discharge cycle, an additional low-current 0.2 C discharge process was followed to discharge the retained capacity within the test battery. The efficiency of high rate dischargeability (HRD) can be calculated by the following equation:

$$HRD_{nc}(\%) = \frac{C_{nc}}{C_{nc} + C_{0.2c}} \times 100\% \quad (2)$$

where C_{nc} denotes the discharge capacity at the discharge current density n C, and $C_{0.2C}$ denotes the discharge capacity of the additional low-current discharge process.

Impedance measurements were carried out after the electrodes were fully activated at 303 K for 5 charge/discharge cycles using a Modulab Electrochemical System of Solartron Analytical. The electrode was charged to a state of charge (*SOC*) of 10% at 0.2 C, and then the *EIS* of the electrode was measured using an AC since perturbation of 5 mV in the frequency range of 1 mHz to 100 kHz. The impedance spectra were calculated and fitted using Zview software. The Tafel and linear polarization curves were measured on the same Modulab electrochemical system by scanning electrode potential at the rate 1mV/s from -1.5 to -0.5V (vs. Hg/HgO) and 0.1 mVs^{-1} from -5 to 5 mV(vs. open circuit potential) at 50% depth of discharge *(DOD)*, respectively.

3. RESULTS AND DISCUSSION

3.1 Characterization of MmNi$_{3.68}$Co$_{0.72}$Mn$_{0.43}$Al$_{0.17}$ hydrogen storage alloy

The XRD pattern of MmNi$_{3.68}$Co$_{0.72}$Mn$_{0.43}$Al$_{0.17}$ hydrogen storage alloy is shown in Fig.1 (a), which demonstrates that the alloy is single-phase alloy with LaNi$_5$ hexagonal structure. The values of hydrogen storage capacity, in term of H/M, and plateau pressure in the hydrogen absorbing process is shown in Fig.1 (b) and fundamental properties of the alloy are listed in Table 2. Desorption equilibrium pressures at 0.6 wt% storage capacity at 303 K, 323 K and 353 K are used to calculate the enthalpy change (ΔH) and entropy change (ΔS) by the following formula：

$$\ln P_{H_2} = \frac{\Delta H}{RT} - \frac{\Delta S}{R} \quad (3)$$

where P_{H_2} is the equilibrium hydrogen pressure, R the gas constant and T the absolute temperature. The calculated enthalpy change and entropy change in the formation of hydride are -32.36 KJ/mol H$_2$ and -102.68 J/(mol· K) H$_2$, respectively. The low ΔH suggests that MmNi$_{3.68}$Co$_{0.72}$Mn$_{0.43}$Al$_{0.17}$ should exhibit high discharge capacity, as the discharge capacity of the alloys increases with the decrease in the magnitude of the change in enthalpy [26].
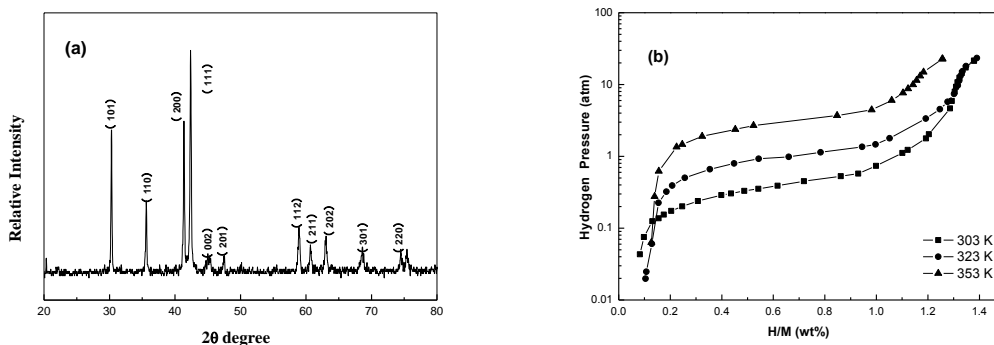
Figure 1. XRD pattern (a) and P-C-T curves of $MmNi_{3.68}Co_{0.72}Mn_{0.43}Al_{0.17}$ alloy sample (b).

Table 2. Fundamental properties of $MmNi_{3.68}Co_{0.72}Mn_{0.43}Al_{0.17}$ alloy used in this experiment

Composition	$MmNi_{3.68}Co_{0.72}Mn_{0.43}Al_{0.17}$	Lattice constant	a=5.0321 Å c =3.9891 Å
Structure	$CaCu_5$	Unit cell volume	87.4765 $Å^3$
Hydrogen uptake	1.38wt% (303K)	Plateau pressure	0.3~0.6 atm (303K)
	1.39wt% (323K)		0.7~1.1 atm (323K)
	1.26wt% (353K)		1.9~3.7atm (353K)
ΔH	-32.36 (KJ/mol H_2)	ΔS	-102.68 (J/(mol·K)

3.2. Discharge behaviors of alloy electrodes in different electrolytes at 303K and 273K

Fig. 2 shows the maximum discharge capacities and dischargeabilities after 50 cycles of $MmNi_{3.68}Co_{0.72}Mn_{0.43}Al_{0.17}$ alloy in the four electrolytes from EO to EL3. The alloy electrodes can be fully activated within 3-4 charge/discharge cycles, and have the similar maximum discharge capacity in the four electrolytes. However, an apparent difference of discharge capacity has been observed after discharged at 0.2 C for 50 cycles. Based on Fig.2, it can be seen that discharge capacity increases from 275.5 mAh/g in EO to 302.6 mAh/g in EL2 and then decrease to 286 mAh/g in EL3 at 303 K, and from 292 mAh/g in EO to 314 mAh/g in EL2 and then decrease to 300 mAh/g in EL3 at 273 K. Obviously, the alloy electrodes in EL2 exhibit the highest maximum discharge capacity and capacity after 50th cycles both at 303 K and 273 K. The addition of 4 wt% LiOH is reasonable for $MmNi_{3.68}Co_{0.72}Mn_{0.43}Al_{0.17}$ alloy to enhance the discharge capacity. In order to illustrate the cycling stability, the capacity retention, S_{50} is calculated and tabulated in Table 3. It shows that the S_{50} increases firstly and then decreases in electrolytes from EO to EL3 both at 303 K and 273 K. Therefore, the dischargeabilities and cycle life of the alloy electrodes were significantly improved by the addition of LiOH into the original electrolyte (EO).
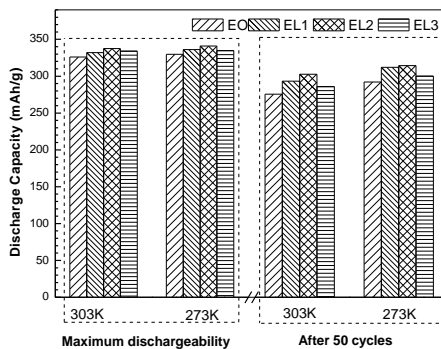
Figure 2. Maximum capacity and capacity after 50 cycles of $MmNi_{3.68}Co_{0.72}Mn_{0.43}Al_{0.17}$ electrodes at 303K and 273K.

Table 3. Discharge properties of $MmNi_{3.68}Co_{0.72}Mn_{0.43}Al_{0.17}$ alloy electrodes in the four electrolytes

Temperature	Electrolyte	C_{max} (mAh/g)	S_{50} (%)	HRD_{750} (%)	HRD_{1500} (%)	R_p (mΩ)	I_0 (mA g^{-1})
303K	EO	326	84.5	82.88	64.34	108	241.85
	EL1	332	88.3	75.98	56.3	113.6	229.7
	EL2	337.6	89.65	72.2	50.4	123.3	211.8
	EL3	334	85.65	68.58	48.1	136.3	191.7
273K	EO	329.6	88.5	75.9	59.02	135	174.4
	EL1	336.2	92.8	60.3	38.6	143.8	163.7
	EL2	340.9	92.2	56.3	35.45	158	148.7
	EL3	334.7	89.7	48.18	12.1	169	139.3

The high-rate dischargeabilities of $MmNi_{3.68}Co_{0.72}Mn_{0.43}Al_{0.17}$ alloy electrodes at different current densities in different electrolytes at 303 K and 273 K are shown in Fig. 3. It can be seen that the HRD decreases from EO to EL3 at 303 K, and this trend is intensified when tested at a low temperature (273 K), or discharged at high current density. For example, the HRD_{1500} decreases from 64.34% in EO to 48.1% in EL3 at 303K, and 59.02% in EO to 12.1% in EL3 at 273K, suggesting that the electrolyte with additional LiOH is adverse to HRD properties of the alloy electrode.
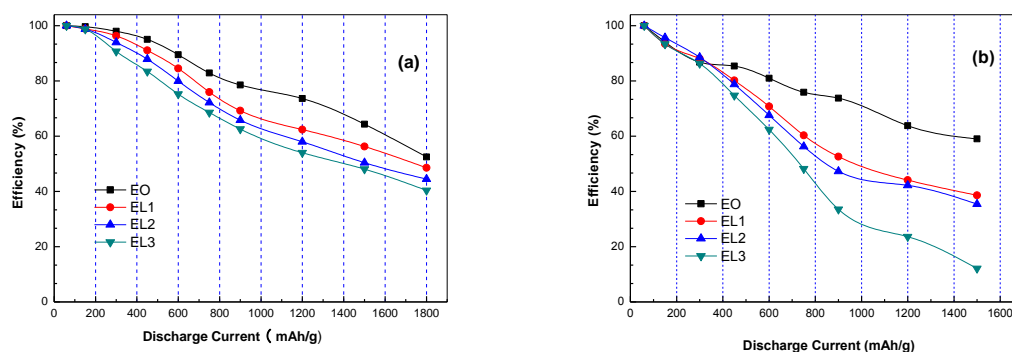

Figure 3. The high rate dischargeability of $MmNi_{3.68}Co_{0.72}Mn_{0.43}Al_{0.17}$ alloy electrodes at: (a) 303k; (b) 273K.

3.3 Corrosion and pulverization characteristics of alloy electrodes in the four electrolytes at 303K

Generally, it is believed that the capacity degradation in Ni-MH batteries are due to corrosion of active components and serious pulverization of the alloy particles [27]. The Tafel polarization measurement was employed to investigate the corrosion behavior of the alloy electrodes in the four electrolytes. The Tafel polarization curves of the alloy electrodes at 50% DOD and 303 K are presented in Fig.4, and the results obtained by Tafel fitting were summarized in Fig.5. The corrosion potential E_{corr} shifts toward a positive direction with increasing additional LiOH concentration in the electrolytes. The negative electrode would be easily corroded with the decreasing of E_{corr}. On the other hand, higher concentration of Li^+ would result in serious corrosion and formation of some oxides related to Li on the surface of the alloy [28]. Affected by the two driving force with opposite directions, the corrosion current I_{corr} firstly decreases and then increases in the electrolytes from EO to EL3. The alloy electrode in EL1 has lower I_{corr}, indicating that the alloy electrode in EL1 has a better anti-corrosion ability and lower corrosion rate. Meanwhile, the alloy electrode in electrolyte EL3 is less corrosion-resistant, and, simultaneously, the discharge capacity decreases severely during the charge/discharge cycle. Based on the capacity retention and corrosion current I_{corr}, it is clearly implied that the oxidation of the active components is not the primary factor in the capacity degradation of the alloy electrodes at the initial stage. In order to study the reason of capacity degradation, the pulverization characteristics of alloy electrodes in different electrolytes are necessarily investigated.
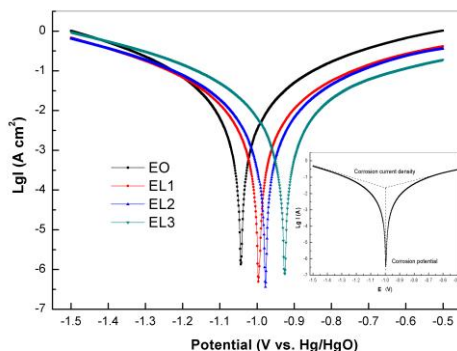

Figure 4. Tafel curves of $MmNi_{3.68}Co_{0.72}Mn_{0.43}Al_{0.17}$ electrodes in different electrolytes at 303 K and a scan rate of 1 mV s^{-1}.
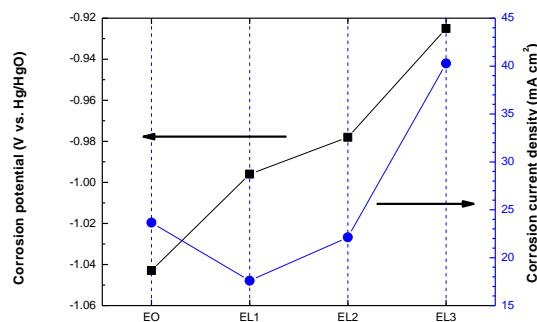

Figure 5. Corrosion potential and corrosion current density in different electrolytes at 303 K.

Due to the volume expansion with the bulk alloy during the charge and discharge cycling, many micro-cracks form in the alloy powders, leading to the pulverization of the particles, as shown in SEM images [28, 29]. However, it is hard to determine the real average particle size of the alloy during the process of electrochemical measurement. Electrochemical impedance spectroscopy (*EIS*) is a powerful tool to get an understanding of different processes if their time constants are well separated, and with *EIS* analyze the oxidation and pulverization process is effectively investigated [18, 30, 31]. The pulverization characteristics of alloy electrodes in the four electrolytes were further studied, and the real surface areas were estimated using *EIS* measurement.
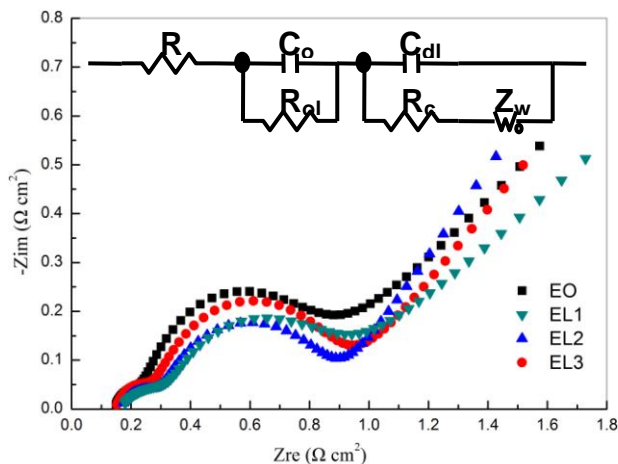

Figure 6. Nyquist plots of EIS spectra of $MmNi_{3.68}Co_{0.72}Mn_{0.43}Al_{0.17}$ electrodes at 10% SOC after activation at 303K; and the equivalent circuit of the alloy electrode using the circuit description code R(QR)(Q(RQ)). R_b: resistance of electrolyte, Q_{ol}: capacitance of the oxide layer, R_{ol}: resistance of the oxide layer, Q_{dl}: double layer capacity, R_{ct}: charge transfer resistance of the interface electrode–electrolyte, Z_W: diffusion impedance of hydrogen.

The electrochemical impedance spectra of $MmNi_{3.68}Co_{0.72}Mn_{0.43}Al_{0.17}$ alloy electrodes in different electrolytes after full activation are presented in Fig.6. Two distinguishable depressed semicircles in different sizes are observed at high-frequency and middle-frequency region respectively, and a straight line at the low frequency region is related to Warburg impedance. The semicircle in the high frequency region is related to the behavior of the oxide layer formed on the alloy surface, and the semicircle in the middle frequency region represents the resistance and capacitance of the charge-transfer process [31]. The proposed equivalent circuit is represented in Fig.6. The constant phase elements Q_{dl} and Q_{ol} with the associated impedance, $Z_{CPE}=1/[Y_{CPE}(j\omega)^n]$ [30, 32-34], are introduced to replace C_{dl} and C_{ol} because of the dispersion phenomena. A_w is the modulus of Z_w, which can be represented in the equation:

$$Z_w = A_w(j\omega)^{-n} \quad (4)$$

where n is the coefficient of the diffusion impedance. By means of the fitting program Zview, the fitting parameters are tabulated in table 4. As shown in table 4, the values of R_{ol} decrease from EO to EL1, and then increase to EL3, which indicates that the anti-corrosion ability of the alloy electrodes

firstly increase, and then decrease from EO to EL3. The alloy electrode in EL1 exhibits better anti-corrosion ability, which is in accordance with I_{corr}.

Table 4. The fitting parameters of the equivalent circuit (CDC: R(QR)(Q(RW)) for EIS spectra of the $MmNi_{3.68}Co_{0.72}Mn_{0.43}Al_{0.17}$ electrode in different electrolytes

Parameter	Q_{ol}		R_{ol} (Ωcm^2)	C_{ol} ($mF\ cm^{-2}$)	Q_{ct}		R_{ct} (Ωcm^2)	Warburg (W)
	Y_{ol} ($\Omega^{-1}s^{-n}cm^{-2}$)	n_{ol}			Y_{ct} ($\Omega^{-1}s^{-n}cm^{-2}$)	n_{ct}		A_W ($\Omega s^{-n}cm^{-2}$)
EO	0.06485	0.712	0.099	8.19	0.2556	0.836	0.522	0.20
EL1	0.05324	0.701	0.091	3.7	0.317	0.841	0.562	0.08
EL2	0.0506	0.678	0.128	2.46	0.375	0.811	0.571	0.06
EL3	0.055	0.667	0.149	4.98	0.483	0.820	0.601	0.10

The capacitance of the oxide film, deduced from the equation $C_{ol}= (Y_{ol}R_{ol})^{1/n}/R_{ol}$, decreases from 8.36 μF cm^{-2} in EO to 2.46 μF cm^{-2} in EL2, and then increases to 4.98 μF cm^{-2} in EL3. C_{ol} is inversely proportional to the thickness d of the oxide layer: $C_{ol}=\varepsilon_0\varepsilon_r S/d$, where $\varepsilon_0\varepsilon_r = 8.85 \times 10^{-13}$ F cm^{-1}. Using magnetic measurements, Ayari [35] has found that the value of the thickness d after activation is estimated at 55 nm. So we can estimate the real surface of alloy powder S and list the results in Fig.7. The real surface of the electrode decreases from 51.95 cm^2 in EO to 15.6 cm^2 in EL2, and then increases to 31.59 cm^2 after fully activated at 303 K. The pulverization of the alloy powders is severer in EO than that of electrolytes with LiOH addition, which accelerates dissolution and diffusion of active elements towards the surface in the alkaline electrolyte, and results in the discharge capacity degradation of the negative electrodes [29]. In order to verify the pulverization difference, the scanning electron microscopy (SEM) observation of the electrodes after 50th cycles in EO and EL2 is presented in fig.7. The bigger particles in EO pulverize to similar average sizes about 2-5 μm. Although many micro-cracks produced in the big particles during the charge/discharge cycle in EL2, the big particles are not pulverized.
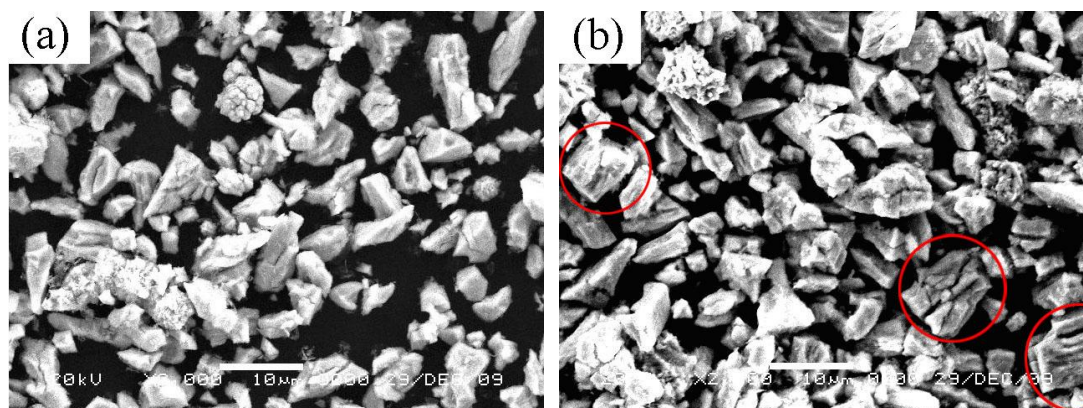

Figure 7. SEM images of MmNi$_5$-based hydrogen storage alloy after 50th cycles in Electrolytes EO (a) and EL2 (b).

Based on the cyclic stability, the values of R_{ol} and the real surface of alloy powder S as shown in Fig.8, it is evident that the capacity degradation of the alloy electrodes in the four electrolytes is primarily ascribed to serious pulverization, other than the oxidation of active components at the initial stage. The improvement on cycle life in EL2 is mainly ascribed to the high pulverization resistance. A similar result was found using XPS analysis [36].

Furthermore, the value of R_{ct} for the alloy electrodes from EO to EL3 are 0.522, 0.562, 0.571 and 0.601 Ωcm^2, respectively. Thus the electrochemical activity of the alloy electrode surface decreases evidently, as a result of the reduction of fresh active surface area during charge/discharge cycles, and serious oxidation on the surface. The value of A_w decreases rapidly from 0.2 in EO to 0.06 in EL2, and then increase to 0.1 in EL3, suggesting a more difficult diffusion of hydrogen in alloy particle in EO than those electrolytes with additional LiOH. The trend of A_w is in accordance with the real surface of alloy powder S. The existence of Li in the electrolytes could enhance penetration of H into the bulk, and decrease the lattice strain during the hydrogen absorption/desorption cycles. Consequently, the pulverization resistances of alloy electrodes are improved. Therefore, the bulk hydrogen diffusion is rather important in the improvement of pulverization resistance of $MmNi_5$-based hydrogen storage alloy.
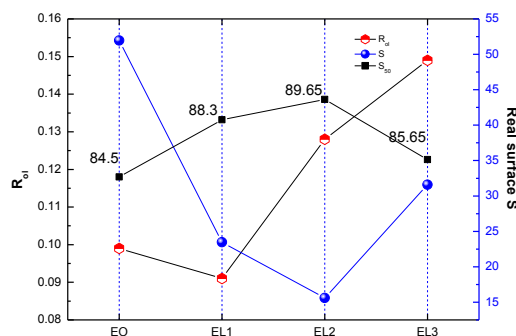

Figure 8. The relationship between capacity retention, $R_{ol,}$ real surface of $MmNi_{3.68}Co_{0.72}Mn_{0.43}Al_{0.17}$ alloy electrodes in the four electrolytes.

3.4 Electrochemical kinetics of the alloy electrodes in the four electrolytes

The exchange current density (I_0) is used to characterize the electrocatalytic activity for charge-transfer reaction on the surface of alloy electrode. Fig.9 shows the linear polarization curves of $MmNi_{3.68}Co_{0.72}Mn_{0.43}Al_{0.17}$ alloy electrodes. Polarization resistance R_p can be obtained from Fig.9, and consequent exchange current density I_0 can be calculated according to the equation:

$$I_0 = \frac{RT}{FR_p} \quad (5)$$

where R is the gas constant, T the absolute temperature and F the Faraday constant. The results obtained are listed in Table 3. It can be seen that the R_p value increases from EO to EL3 at both 303K

and 273K, which is in agreement with R_{ct} as EIS study. Consequently, I_0 decreases from EO to EL3. It is well known that the fresh active surface area and oxide layer on the surface of alloy particles should be principally responsible for the electrocatalytic activity of alloy electrode. The pulverization resistances are improved with LiOH addition, resulting in the reduction of fresh active surface area. The serious corrosion of alloy electrode in EL3 further depresses the electrocatalytic activity, and results in the decrease of exchange current density I_0. Iwakura [38] has pointed out that the high-rate dischargeability is controlled by kinetics, of the charge transfer at the surface and the hydrogen diffusion in the bulk. Based on the results of HRD, exchange current density and A_w, it can be inferred that the charge-transfer reaction on alloy surface is the rate-determining step when tested at 273 K and 303 K.
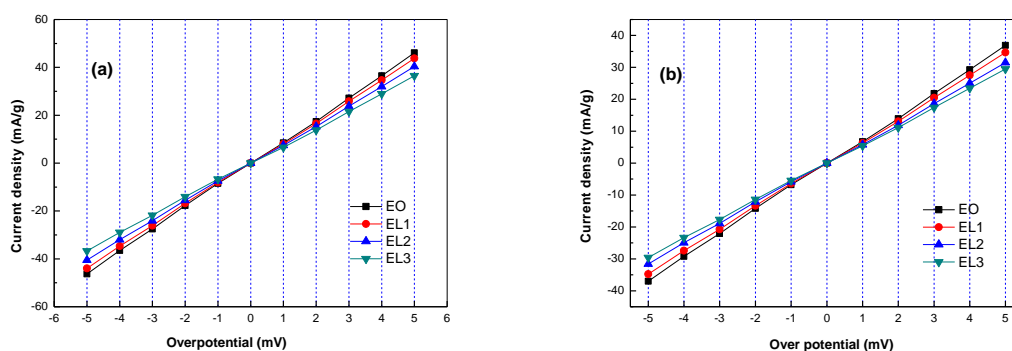

Figure 9. Exchange-current density I_0 of MmNi$_{3.68}$Co$_{0.72}$Mn$_{0.43}$Al$_{0.17}$ hydrogen storage alloy electrodes at 303 K (a); and 273 K (b).

4. CONCLUSION

1）   The electrolytes with additional LiOH take notable positive effect on the discharge capacity and cycle life of alloy electrodes at both 303 K and 273 K. The alloy electrodes in EL2 exhibit the highest maximum discharge capacity and capacity after 50th cycles both at 303 K and 273 K, and the reasonable addition of LiOH is 4 wt% for MmNi$_{3.68}$Co$_{0.72}$Mn$_{0.43}$Al$_{0.17}$ alloy to enhance the discharge capacity.

2）   The corrosion current I_{corr} and resistance of the oxide layer R_{ol} firstly decreases and then increases in the electrolytes from EO to EL3, indicates that the alloy electrode in EL1 has a better anti-corrosion ability and lower corrosion rate.

3）   With *EIS* analysis the pulverization process is investigated. The real surface of the electrode decreases from 51.95 cm^2 in EO to 15.6 cm^2 in EL2, and then increases to 31.59 cm^2 after fully activated at 303K. The existence of Li in the electrolytes could enhance penetration of H into the bulk, and decrease lattice strain during the hydrogen absorption/desorption cycles, which improve the pulverization resistance of alloy electrodes.

4）   The capacity degradation of the alloy electrodes in the four electrolytes is primarily

ascribed to serious pulverization, other than the oxidation of active components at the initial stage. The electrocatalytic activity of alloy electrode surface is principally responsible for the high rate dischargeability, which decreasing gradually from EO to EL3，and the charge-transfer reaction on alloy surface is the rate-determining step at both temperatures 303 K and 273 K.

References

1. M. V. Ananth, M. Ganesan, N. G.Renganathan and S. Lakshmi, *Int. J. Hydrogen Energy*, 34 (2009) 356.
2. D. Endo, K. Sakaki and E. Akiba, *J. Alloys Compd.*, 459 (2008) 215.
3. H. Ye, B.J. Xia, W.Q. Wu, K. Du and H. Zhang, *J. Power Sources*, 111 (2002) 145.
4. Z.M. Wang, Li CYV and Chan SLI, *J. Alloys Compd.*, 438 (2007) 298.
5. X.D. Liu, Hongwei Feng, Xiao Tian, Bo Chi, Shufang Yan and Jin Xu, *Int. J. Hydrogen Energy*, 34(17) (2009) 7291-7295.
6. M. Raju, M. V. Ananth and L. Vijayaraghavan, *Electrochimica Acta*, 54 (2009) 1368.
7. M.V. Ananth, M. Raju, K. Manimaran, G. Balachandran and L.M. Nair, *J. Power Sources*, 167 (2007) 228.
8. H.B. Yang, H. Fukunaga, T. Ozaki, T. Iwaki, S. Tanase and T. Sakai, *J. Power Sources*, 133 (2004) 286.
9. Z.H. Ma, J.F. Qiu, L.X. Chen and Y.Q. Lei, *J. Power Sources*, 125 (2004) 267.
10. Z.L. Zhou, Y.Q. Song, S. Cui, C.G. Huang, W.L. Qian, C.G. Lin, Y.J. Zhang and Y.L. Lin, *J. Alloys Compd.*, 501 (2010) 47.
11. H. Miao, H.G. Pan, S.C. Zhang, N. Chen, R. Li and M.X. Gao, *Int. J. Hydrogen Energy*, 32 (2007) 3387.
12. J.X. Ma, H.G. Pan, C.P. Chen and Q.D. Wang, *J. Alloys Compd.*, 343 (2002) 164.
13. H.G. Pan, J.X. Ma and C.S. Wang, *Electrochimica Acta*, 44 (1999) 3977.
14. S. Bliznakov, E. Lefterova, N. Dimitrov, K. Petrov and A. Popov, *J. Power Sources*, 176 (2008) 381.
15. C. Khaldi, S. Boussami, B.B. Rejeb, H. Mathlouthi and J. Lamloumi, *Mater. Sci. Eng. B*, 175 (2010) 22.
16. C. Rongeat, M.H. Grosjean, S. Ruggeri, M. Dehmas, S. Bourlot, S. Marcotte and L.Roué, *J. Power Sources*, 158 (2006) 747.
17. X.Y. Zhao, Y. Ding, M. Yang and L.Q. Ma, *Int. J. Hydrogen Energy*, 33 (2008) 81.
18. C. Khaldi, H. Mathlouthi and J. Lamloumi, *J. Alloys Compd.*, 469 (2009) 464.
19. X.Y. Zhang, Y.G. Chen, M.D. Tao and C.L. Wu, *J. Rare Earth*, 26 (2008) 402.
20. Z.M. Wang, Li CYV and Chan SLI, *Int. J. Hydrogen Energy*, 34 (2009) 5422.
21. Z.M. Wang, P.J. Tsai, Chan SLI, H.Y. Zhou and K.S. Lin, *Int. J. Hydrogen Energy*, 35 (2010) 2033.
22. H.H. Uchida, Y. Ozu, K. Suzuki, S. Kubo and A. Yoshizawa, *J. Alloys Compd.*, 293 (1999) 369.
23. H.H. Uchida, K. Suzuki, S. Kubo and H. Kondo, *Int. J. Hydrogen Energy*, 24 (1999) 879.

24. Y. Ozu, T. Kuji and H. Uchida, *J. Alloys Compd.*, 330-332 (2002) 632.
25. C.Y. Ni, H.Y. Zhou, N.L. Shi and Z.M. Wang, *Electrochimica Acta*, 59 (2012) 237.
26. X.B. Ma, X.D. Wei, H. Dong and Y.M. Liu, *J. Alloys Compd.*, 490 (2010) 548.
27. V.A. Yartys, A.B. Riabov, R.V. Denys, M. Sato and R.G. Delaplane, *J. Alloys Compd.*, 408-412 (2006) 273.
28. Z. Zhen, Y. Jie, Y.X. Li, D.Y. Song and Y.S. Zhang, *J. Power Sources*, 72 (1998) 236.
29. G.Y. Shang, S.M. Han, J.S. Hao, Y. Liu, X.L. Zhu, Y. Li and D.Y. Xue, *J. Alloys Compd.*, 493 (2010) 573.
30. X.Y. Zhao, L.Q. Ma, Y. Ding and X.D. Shen, *Int. J. Hydrogen Energy*, 34 (2009) 3389.
31. C. Khaldi, H. Mathlouthi and J. Lamloumi, *J. Alloys Compd.*, 479 (2009) 284.
32. H. Yang, Y.G. Chen, M.D. Tao, C.L. Wu, J. Shao and G. Deng, *Electrochimica Acta*, 55 (2010) 648.
33. W.X. Chen. *J. Power Sources*, 92 (2001) 102.
34. M. Sánchez, J. Gregori, C. Alonso, J.J. García-Jareño, H. Takenouti and F. Vicente, *Electrochimica Acta*, 52 (2007) 7634.
35. J.B. Jorcin, M.E. Orazem, N. Pébère and B. Tribollet, *Electrochimica Acta*, 51 (2006) 1473.
36. M. Ayari, V. Paul-Boncour, J. Lamloumi, A. Percheron-Guégan and M. Guillot, *J. Magn. Magn. Mater.*, 288 (2005) 374.
37. Y.F. Liu, Y.H. Cao, L. Huang, M.X. Gao and H.G. Pan, *J. Alloys Compd.*, 509 (2011) 675.
38. C. Iwakura, T. Oura, H. Inoue and M. Matsuoka, *Electrochimica Acta*, 41 (1996) 117.